International Journal of Applied Earth Observations and Geoinformation 96 (2021) 102276

Contents lists available at ScienceDirect

International Journal of Applied Earth Observations and Geoinformation

journal homepage: www.elsevier.com/locate/jag

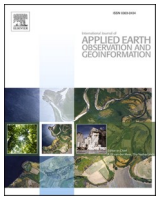

Diurnal variation of sun-induced chlorophyll fluorescence of agricultural crops observed from a point-based spectrometer on a UAV

Na Wang [a,*], Juha Suomalainen [b], Harm Bartholomeus [a], Lammert Kooistra [a], Dainius Masiliūnas [a], Jan G.P.W. Clevers [a]

[a] Laboratory of Geo-Information Science and Remote Sensing, Wageningen University and Research, P.O. Box 47, 6700 AA Wageningen, the Netherlands
[b] Finnish Geospatial Research Institute, National Land Survey of Finland, Geodeetinrinne 2, 02430 Masala, Finland

ARTICLE INFO

Keywords:
Sun-induced chlorophyll fluorescence
Crop traits
Diurnal patterns
Unmanned Aerial Vehicle

ABSTRACT

Unmanned Aerial Vehicle (UAV)-based measurements allow studying sun-induced chlorophyll fluorescence (SIF) at the field scale and can potentially upscale results from ground to airborne/satellite level. The objective of this paper is to present the FluorSpec system providing SIF measurements at the field level onboard a UAV, and to evaluate the potential of this system for understanding diurnal SIF patterns for different arable crops. The core components of FluorSpec are a point spectrometer configured to measure in the O_2 absorption bands at sub-nanometer resolution, bifurcated fibre optics to switch between the downwelling irradiance and upwelling radiance measurements, and a laser range finder allowing accurate atmospheric correction. The processing chain is explained and the capability of the novel Spectral Shape Assumption Fraunhofer Line Discrimination (SSA-FLD) method to retrieve SIF was tested. To test the reliability of FluorSpec diurnal SIF measurements, near-canopy diurnal SIF was monitored during the growing season over potato and sugar beet plants with a ground-based setup. The two crops exhibited a clear diurnal SIF pattern, which positively correlated with the photosynthetically active radiation (PAR). The divergence in diurnal patterns between SIF and PAR indicated that the crops might be suffering from heat stress. A significant correlation between SIF and the Photosystem II Quantum Yield was obtained. By mounting the FluorSpec on a UAV, SIF measurements were obtained over the same crops during a clear day. UAV-based SIF also exhibited a pronounced diurnal pattern similar to the ground-based measurements and it showed clear spatial variation within different crop fields. The obtained results demonstrate the ability of the FluorSpec system to reliably measure plant fluorescence at ground and field level, and the possibility of the UAV-based FluorSpec to bridge the scale gap between different levels of SIF observations.

1. Introduction

The rapid increase in food demand will be one of the greatest challenges in the following decades (Foley et al., 2011). Although over the past decades, yield levels have improved considerably, the quantity of photosynthesis places an upper limit to food production (Guanter et al., 2014). Crop productivity is generally not determined by the potential activity of the photosynthetic system, but by the actual one since the photosynthetic activities are affected by many adverse environmental stress factors, such as lack of water or nutrients. These can weaken the photosynthetic apparatus, causing a decrease of plant productivity and overall crop yield (Kalaji et al., 2016, 2017). Light energy absorbed by leaf chlorophyll may be used for photochemistry, dissipated thermally, or is reemitted as chlorophyll fluorescence (ChF). Thus, as a by-product of photosynthesis, ChF has been proven to be a direct proxy for the instantaneous photosynthetic rate related to vegetation stress conditions (Smorenburg et al., 2002; Zarco-Tejada et al., 2016).

In the last decade, sun-induced chlorophyll fluorescence (SIF), which is produced in natural daylight and can be detected with remote sensing techniques, has been a research focus to understand vegetation photosynthesis at a large scale. Maier et al. (2004) showed the potential of SIF as a new tool for precision farming with remote sensing techniques. Intensive ground-based studies have shown the potential of SIF as an indicator of crop photosynthesis (Goulas et al., 2017; Rascher et al., 2009). Several SIF studies over crop canopies have confirmed a positive correlation between crop SIF and water stress (Daumard et al., 2010; Xu et al., 2018). The sensitivity of SIF to vegetation phenology and its diurnal and seasonal dynamics have also been explored in several

* Corresponding author.

https://doi.org/10.1016/j.jag.2020.102276
Received 24 June 2020; Received in revised form 25 November 2020; Accepted 27 November 2020
Available online 18 December 2020

studies (Cogliati et al., 2015; Daumard et al., 2012; Li et al., 2020; Meroni et al., 2011; Wyber et al., 2017).

Recently, important improvements in sensor capabilities and further understanding of the contribution from fluorescence to apparent reflectance have made it achievable to measure SIF from space, using platforms/instruments such as the Global Ozone Monitoring Instrument-2 (GOME-2) (Joiner et al., 2013), the Greenhouse Gases Observing Satellite (GOSAT) (Frankenberg et al., 2011), the Orbiting Carbon Observatory (OCO-2) (Frankenberg et al., 2014), and the TROPOspheric Monitoring Instrument (TROPOMI) (Guanter et al., 2015). A growing body of literature has recognized the potential of satellite-based SIF as an indicator of photosynthetic activities at large scale by monitoring global SIF patterns and dynamics (Frankenberg et al., 2014). Damm et al. (2010) showed that including SIF into gross primary productivity (GPP) modeling improves their results in predicting diurnal courses of GPP for agricultural fields. Similar conclusions were also found by Guan et al. (2016), who showed that spaceborne SIF retrievals from GOME-2 can improve the monitoring of crop productivity by including SIF into GPP models. Furthermore, airborne systems have been developed to upscale crop SIF from canopy to satellite level. For example, the airborne system HyPlant is able to map SIF at an intermediate spatial resolution (e.g., 0.5 m*1m with a flying height of 350 m above ground level (AGL)), showing that there are large variations in SIF between different vegetation types (Rascher et al., 2015). Zarco-Tejada et al. (2016) found that, compared to other selected structural and physiological indices, SIF quantified from airborne hyperspectral imagery was the most robust indicator of photosynthesis measured by assimilation rates.

To further explore the potential of SIF in agriculture, especially in precision agriculture, a fine spatial resolution is playing a key role. For ground-based set-ups, the distance between measured targets and instruments ranges from 0.1 m to 10 m above the canopy (Cheng et al., 2013; Cogliati et al., 2015; Yang et al., 2018). Thus, with these set-ups, the SIF signal of only a few individual plants can be monitored, making measurements at the field, ecosystem, or global scales infeasible. For satellite observations, the signals observed are mixed due to the low spatial resolution (typically between a few up to tens of kilometers), which is an issue especially for the monitoring of small-scale farmlands. Although intermediate-scale observations using airborne imaging spectroscopy are critical to bridge the existing gap between small-scale field and global observations, the validation of airborne SIF products is still essential, as multiple factors can influence SIF measurements. Ground-based SIF observations, such as the FLOX system (FloX, JB Hyperspectral, Dusseldorf, Germany, PhotoSpec), provide a way to validate airborne SIF, but it is challenging to compare it with airborne SIF due to the large difference in their footprints. Additionally, imagery obtained from airborne sensors can only be evaluated at a limited number of locations measured by ground-based systems (Tagliabue et al., 2019).

Therefore, remotely sensed data acquired at the field level are highly needed to facilitate SIF interpretation in agricultural fields and to bridge the gap between the proximal level to the airborne level. Unmanned Aerial Vehicles (UAVs) are versatile platforms that have a potential to acquire SIF at a low flying altitude (from 10 to 120 m). UAVs can also acquire data at high temporal resolution on specific areas, e.g. diurnal measurements, and thus support airborne and satellite-based measurements through validation and interpretation. Additionally, UAVs can be more cost-effective at small scale and have great potential for applications in precision agriculture and phenotyping (Camino et al., 2019). Accurate SIF retrieval requires spectroradiometers with an ultrafine spectral resolution (less than 1 nm for far-red SIF and less than 0.5 nm for red SIF) and high signal-to-noise ratio (SNR) (Rossini et al., 2016). Simultaneous acquisitions of sunlight irradiance (downwelling) and target radiance (upwelling) also play a significant role in the precision of SIF measurements (MacArthur et al., 2014). Non-imaging spectrometers with technical advancements, including reduced size, high SNR, high spectral and temporal resolutions, has encouraged the development of UAV-based SIF payloads (MacArthur and Robinson, 2015).

So far, few studies have focused on UAV-based SIF with non-imaging spectrometers. Garzonio et al. (2017) developed the HyUAS equipped with a non-imaging instrument (USB4000) and a high-resolution RGB camera, based on a small rotary-wing UAV, to measure reflectance and SIF. Their study was mainly to test this new development and for provision of a more homogeneous footprint at a given flight height while flying over different vegetation canopies around solar noon. Piccolo Doppio, a dual-field-of-view spectrometer system consisting of two Ocean Insight spectrometers (QE Pro and FLAME) for reflectance and fluorescence measurements, was introduced by MacArthur et al. (2014) and was used aboard a DJI Matrice 600 pro UAV using a fly-and-hover approach (Maseyk et al., 2018) to gain insight into canopy-level photosynthetic responses to CO_2. However, this experiment was performed on woodland, not on crops. A case study of alfalfa and grass canopies was carried out with the AirSIF system, a dual-field-of-view spectroradiometer system in which sensor etaloning and platform motion correction was introduced to achieve accurate geolocation and shape reconstruction of the SIF measurements (Bendig et al., 2019). Aside from these studies, no studies have currently been done towards the application of this setup to measure SIF in precision agriculture and the diurnal cycles of SIF over different crop canopies to characterize variation of photosynthesis-related processes over the day.

This paper presents the FluorSpec system that includes a non-imaging sub-nanometer spectrometer operating across the visible and near-infrared spectral region. This system can be used both at a fixed location to acquire ground-based SIF measurements at the canopy level at high temporal frequency as well as be used as a UAV-based payload to acquire SIF data at the plot or field level. The main goal of this study is to evaluate the potential of this UAV-based spectroscopy approach for understanding crop SIF and photosynthesis in precision agriculture at the field level and to contribute to bridging the gap in SIF measurements between ground and airborne/spaceborne scales. Diurnal SIF measurements at ground and field level were collected over potato and sugar beet fields as case studies.

2. FluorSpec system

2.1. System design

The FluorSpec system is composed of a non-imaging hyperspectral spectrometer (Ocean Insight QE-Pro), spectrometer optics, a simple USB connected Global Navigation Satellite System (GNSS) receiver, a laser rangefinder sensor (LightWare SF11C), a Raspberry Pi data sink, custom synchronization electronics, and a lithium polymer battery (3S, 500–1000 mA). Fig. 1 shows the technical details of the system. We designed the FluorSpec to be mounted on board an octocopter UAV, but it is basically a stand-alone set-up that can be installed on any platform able to carry a 2.0 kg payload.

The QE-Pro is a compact, actively cooled, high-performance spectrometer that weighs 1.15 kg. The spectrometer unit selected for FluorSpec is configured to the wavelength range of 630–800 nm with a spectral resolution of 0.3 nm (FWHM). The spectrometer observes light through a bifurcated optical fibre, which has one tip connected to upward looking irradiance optics and the second one to downward looking custom radiance optics (Fig. 1). The irradiance optics consist of an optical fibre mount, servo driven shutter, and a diffuser providing a near-Lambertian field-of-view (FOV). Similarly, the downward looking radiance optics consist of a fibre mount, a shutter, and an open “lens tube” (Thorlabs SM05 series) restricting the spectrometer FOV to 25° opening angle. Optionally, also a simple lens can be installed on the lens tube to limit the FOV to a narrower angle. With the servo-controlled shutters the system can automatically switch between irradiance, radiance, and dark current measurement modes.

The system is controlled in real time by a Raspberry Pi 2 computer. The control software of the FluorSpec is written in PHP as a customized

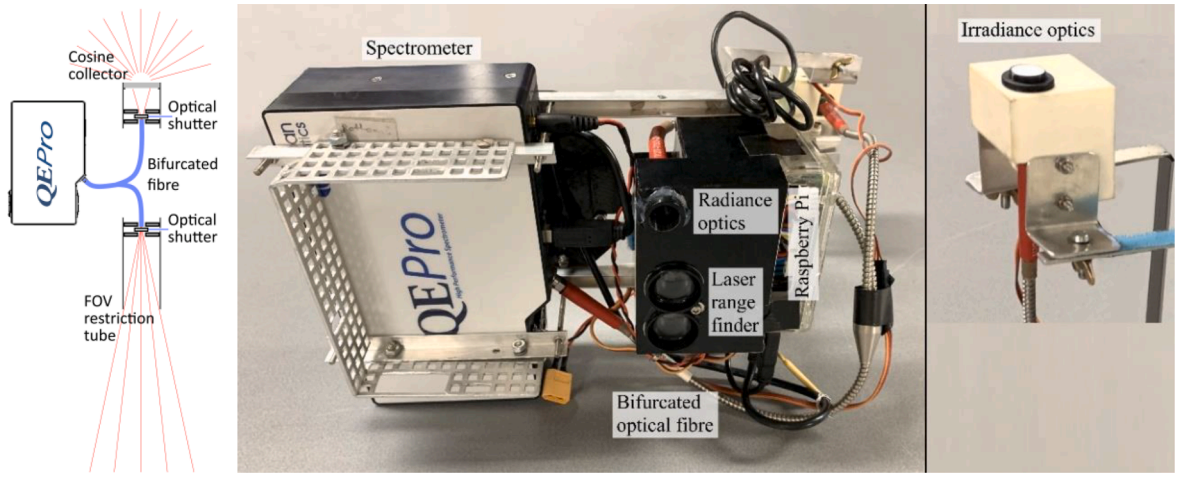

Fig. 1. Schematic drawing of the FluorSpec optics and photos of the system.

version of the Ocean Optics STS Dev Kit software. In measurement mode, the FluorSpec repeats a loop where it measures a dark current spectrum, an irradiance spectrum, and a radiance spectrum. Simultaneously, it records the data streams from GNSS receiver and laser range finder. These metadata define the system geographical position, provide absolute timing, and provide an accurate above-ground altitude. To output the data, the raw spectra, geo-location data and metadata are written to a USB thumb drive as an ASCII file, which can then be post-processed to final SIF data according to the processing steps described in Section 2.3.

2.2. Sensor calibration

Sensor calibration is required to produce absolute irradiance and radiance values. In addition, the accuracy of the reflectance factors and absolute values of reflected and fluorescent radiance are directly dependent on the accuracy of the radiance sensor calibration. The measured irradiance was calibrated using direct solar irradiance at sea level. Since pairing of the measured spectrum accurately is hard, the spectral resolutions of both sensors need to be the same to get a high calibration accuracy. Therefore, a spectral smoothing function on both spectra was performed by running a Gaussian averaging filter. After that, the radiance sensor can be calibrated with the radiometric measurements from a white Spectralon panel (99%) and from the calibrated irradiance sensor.

2.3. Processing chain

The processing chain is based on MATLAB (v2018b, Mathworks) scripts, including steps for radiometric processing of spectra, merging each spectrum, processing laser rangefinder and GPS data, atmospheric correction, and SIF retrieval method.

2.3.1. Radiometric processing

As the ChF is a measurement in absolute radiance units, the first step of the FluorSpec processing chain is to convert the acquired raw spectra (digital numbers) to at-sensor irradiance (Wm^{-2} nm^{-1}) and radiance (Wm^{-2} sr^{-1} nm^{-1}). This is done by removing the dark current (interpolated from preceding and following measurement) and by multiplying the digital number values with the radiometric calibration coefficient per wavelength. Next, the at-sensor irradiance and radiance are converted to their top-of-canopy (TOC) equivalents by applying an atmospheric correction which is described in Section 2.3.2. Afterwards, to get the TOC irradiance at the same time as the TOC radiance measurement, preceding and following TOC irradiances are linearly interpolated to the GPS time stamp of the corresponding TOC radiance measurement.

2.3.2. Atmospheric correction

The at-sensor irradiance and radiance must be converted to their top-of-canopy equivalents by applying an atmospheric correction. Since SIF accounts for less than 2% of the reflected radiance into the sensor and the atmosphere under the measurement altitude distorts the observed SIF signal, an atmospheric correction is critical for any accurate airborne fluorescence measurements. In this study, SIF is retrieved using the spectral region around the 760 nm O_2-A absorption feature, where the atmosphere has a high impact on the radiance. We used the *MODerate resolution atmospheric TRANsmission* (MODTRAN) algorithm to simulate the transmittance profile through the bottom 1 km of the atmosphere around the 760 nm O_2-A feature as sensed by a sensor with 0.1 nm spectral resolution (Fig. 2). To simulate the atmospheric transmittance of the bottom 1 km of atmosphere, standard MODTRAN parameters (mid-latitude summer atmospheric profile, rural aerosol type, visibility = 23 km, sensor altitude = 1 km, and default values for water column, CO_2 and ground temperature) (MODTRAN®, Spectral Sciences, Inc) were used in the MODTRAN model.

To get a useful transmittance for a specific UAV altitude, the simulated transmittance can be converted to different thicknesses of the atmosphere ($T(d)$) using the Beer-Lambert law:

$$T(d) = \left[T\left(d_{ref}\right)\right]^{\frac{d}{d_{ref}}} \quad (1)$$

where d is the distance light goes through the atmosphere (i.e. UAV

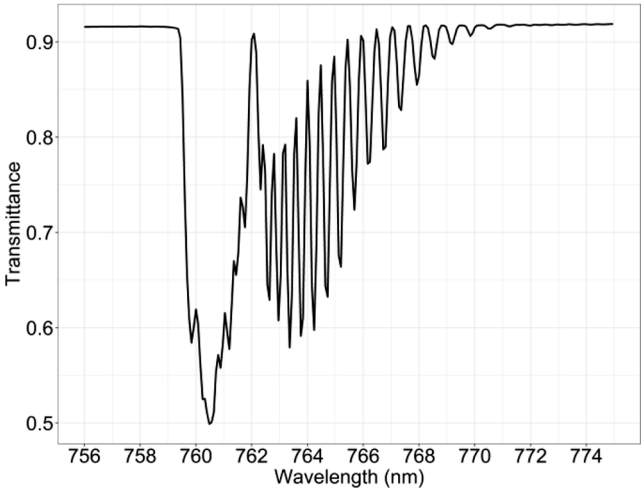

Fig. 2. The transmittance of the bottom 1 km of atmosphere around the 760 nm O_2-A absorption feature as simulated using MODTRAN.

altitude above ground level), d_{ref} is the distance used in the simulation (1 km), and $T(d_{ref})$ is the simulated transmittance.

If we consider only atmospheric transmittance, but no additive scattering, the measured at-sensor radiance (L_{sensor}) and irradiance (E_{sensor}) can be converted to their TOC equivalents (L_{toc}, E_{toc}) using:

$$L_{toc}(\lambda) = L_{sensor}(\lambda) \Big/ \left[T\left(d_{ref},\lambda\right)\right]^{\frac{d}{d_{ref}}} \quad (2)$$

$$E_{toc}(\lambda) = (E_{sensor}(\lambda))^{*}\left[T\left(d_{ref},\lambda\right)\right]^{\frac{h}{d_{ref}}} \quad (3)$$

where d is the distance between the target and the radiance sensor and h is the above-canopy altitude of the irradiance sensor.

Using equations (2) and (3), we converted the at-sensor spectra to their TOC equivalents. With the FluorSpec system, d is directly measured by the laser rangefinder sensor. In downward looking measurements using this same value works also as h.

2.3.3. The SIF retrieval method (SSA-FLD)

The Fraunhofer Line Discriminator (FLD) principle has long been applied as the reference method to disentangle the SIF signal from the reflectance signal (James and Plascyk, 1975; Moya et al., 2004; Plascyk and Gabriel, 1975). The standard FLD-based approach utilizes two spectral bands to estimate fluorescence around each of the oxygen absorption features (O_2-B at 687 nm and O_2-A at 760 nm): one band inside and one band outside the absorption feature. A fundamental assumption of this method is that reflectance and fluorescence remain constant over the absorption feature of interest. In our study, spectra were acquired using the QE-pro spectrometer, which has an ultra-high spectral resolution (0.3 nm). To make full use of the spectral information within the oxygen absorption regions, we apply a slightly adapted FLD-based approach to retrieve SIF, called Spectral Shape Assumption FLD (SSA-FLD). Different from FLD assumptions of constant reflectance and fluorescence over the absorption feature, SSA-FLD employs a linear function to represent reflectance and a known shape of the fluorescence spectrum to describe the chlorophyll fluorescence over the spectral region around O_2-A absorption feature, where the amount of incoming radiation is more comparable to the fluorescence emission. The spectral fitting method (SFM) is another advanced technique to retrieve the fluorescence and reflected radiance from high spectral resolution radiance observations (Mazzoni et al., 2012; Meroni et al., 2010). The method relies on proper mathematical functions representing the surface reflectance (e.g. linear, polynomial, or piecewise cubic splines functions) and the chlorophyll fluorescence (e.g. Lorentzian, Gaussian or Voigt functions) within narrow spectral windows confined to the oxygen absorption bands. Therefore, SSA-FLD can be regarded as a special case of SFM. In a parallel study we compared the two methods, and they were strongly linearly correlated ($R^2 = 0.99$) and therefore we decided to continue with SSA-FLD (results not shown).

The TOC radiance (L_{toc}) leaving the target can be written as a combination of the traditional reflected radiance and the fluorescence radiance (L_{fl}) components:

$$L_{toc}(\lambda) = \frac{1}{\pi}E_{toc}(\lambda)R'_{target}(\lambda) + L_{fl}(\lambda) \quad (4)$$

where $E_{toc}(\lambda)$ is the TOC incident irradiance hitting the target and R'_{target} is the apparent reflectance factor of the target without fluorescence effects.

The only two unknown items in equation (4) are $R'_{target}(\lambda)$ and $L_{fl}(\lambda)$. To solve the fluorescent radiance component, the SSA-FLD model uses two assumptions. Firstly, it assumes that the fluorescence follows a known shape of the fluorescence spectrum and, secondly, that the reflectance factor spectrum of the target object behaves linearly over the used spectral region.

Thus, we split the chlorophyll fluorescent radiance ($L_{fl}(\lambda)$) into a known spectral shape component ($l_{fl}(\lambda)$) and an unknown amplitude component ($\widehat{L}_{fl}$):

$$L_{fl}(\lambda) = \widehat{L}_{fl}l_{fl}(\lambda) \quad (5)$$

For convenience, we can decide to scale the shape component so that $[l_{fl}(\lambda_{760nm}) = 1]$ and $[\widehat{L}_{fl} = L_{fl}(\lambda_{760nm})]$.

Similarly, we need to split the reflectance factor of the target into a known spectral shape component ($r_{target}(\lambda)$ and an unknown amplitude component ($\widehat{R}_{target}$):

$$R_{target}(\lambda) = \widehat{R}_{target}r_{target}(\lambda) \quad (6)$$

To follow the assumption that the reflectance factor changes linearly over the oxygen absorption feature, we must solve the reflectance factor on both sides of it using equation:

$$R_{target}(\lambda) = \pi\frac{L_{target}(\lambda)}{E_{toc}(\lambda)} \quad (7)$$

and then linearly interpolate the $r_{target}(\lambda)$spectrum for all sampled wavelengths in the gap area. In principle, at this stage we could solve also $\widehat{R}_{target}$ but by solving only the shape component now $r_{target}(\lambda)$ improves the retrieval accuracies of both $\widehat{R}_{target}$ and $\widehat{L}_{fl}$ in the final solution stage.

By inserting Equations (5) and (6) into Equation (4), we get:

$$L_{toc}(\lambda) = \frac{1}{\pi}E_{toc}(\lambda)\widehat{R}_{target}r_{target}(\lambda) + \widehat{L}_{fl}l_{fl}(\lambda) \quad (8)$$

which can be rearranged so that all wavelength-dependent components (which are known) are separated from the non-wavelength-dependent components (which are unknown):

$$\left(\frac{L_{toc}(\lambda)}{l_{fl}(\lambda)}\right) = \widehat{R}_{target}\left(\frac{E_{toc}(\lambda)r_{target}(\lambda)}{\pi l_{fl}(\lambda)}\right) + \widehat{L}_{fl} \quad (9)$$

This is the main equation that SSA-FLD uses to solve the fluorescent radiance from observations. The equation has two unknown parameters, $\widehat{R}_{target}$ and $\widehat{L}_{fl}$, which could be solved simply by using data points at two or more wavelengths. In a computer environment, the $\widehat{R}_{target}$ and $\widehat{L}_{fl}$ are solved best using the full spectral information over the oxygen absorption band by writing the equation in matrix representation with wavelengths incrementing horizontally in the matrix cells.

By filling the matrices with the spectra over the oxygen absorption area (for example ± 5 nm), we can linearly solve the unknown parameters by matrix division:

$$\left[\widehat{R}_{target} \quad \widehat{L}_{fl}\right] = \frac{M_1}{M_2} \quad (10)$$

where

$$M_1 = \left[\frac{L_{toc}(\lambda_1)}{l_{fl}(\lambda_1)}, \quad \frac{L_{toc}(\lambda_2)}{l_{fl}(\lambda_2)}, \quad \cdots\right] \quad (11)$$

$$M_2 = \begin{bmatrix} \frac{E_{toc}(\lambda_1)r(\lambda_1)}{\pi l_{fl}(\lambda_1)}, & \frac{E_{toc}(\lambda_2)r(\lambda_2)}{\pi l_{fl}(\lambda_2)}, & \cdots \\ 1, & 1, & \cdots \end{bmatrix}$$

After $\widehat{L}_{fl}$ has been solved, it can be converted to the full fluorescence radiance spectrum ($L_{fl}(\lambda)$) using equation (5).

2.3.4. SIF normalization

The vegetation produces fluorescence relative to the amount of the incident photosynthetically active radiation (PAR irradiance, E_{PAR}) in energy units (μmol m^{-2} s^{-1}), which designates the spectral range of solar radiation from 400 to 700 nm. The variation in PAR absorbed by a canopy caused by different illumination conditions for a closed canopy

can be considered by normalizing SIF by incident PAR (Daumard et al., 2012). Furthermore, the normalized SIF can provide more insights in the effects of pigments, leaf area, leaf inclination and physiology to variations of SIF (van der Tol et al., 2016). The normalized SIF only represents the emission efficiency at the O_2-A band (760 nm), and only in one solid angle, therefore its unit is $\mu m^{-1} sr^{-1}$. Normalized SIF ($SIF_{normalized}$) can be expressed as

$$SIF_{normalized} = \frac{L_{fl}(760nm)}{E_{PAR}} \quad (12)$$

3. Case studies

3.1. Study areas

There were two study sites in our case studies. The main study site (study site 1) was located in the agricultural experimental research fields of Unifarm, Wageningen University & Research (51.987°N, 5.652°E), north to the city of Wageningen, the Netherlands. The second study site (study site 2) was a grassland field on the Campus of Wageningen University. The average altitude of the study areas is 7 m above mean sea level. The mean annual precipitation is 568 mm and the mean annual temperature is 10 °C.

Within study site 1, several crops like sugar beets (*Beta vulgaris* L., variety Urselina) and potato (*Solanum tuberosum* L., variety Aventra) were grown by using common field rotation practices (Fig. 3). One sugar beet field (2.30 ha) and one potato field (1.22 ha) were selected as experimental targets for both ground and UAV measurements. Sugar beets grew in 2018 from April 19 (day of year (DOY): 109) to November 7 (DOY 311), and potato was planted on April 13, 2018 (DOY 103) and harvested on August 28, 2018 (DOY 240). All observations with the FluorSpec system took place under clear sky conditions while the canopies of both crops were fully closed.

3.2. FluorSpec measurements for radiometric sensor calibration

The FluorSpec irradiance sensor was calibrated using the direct component of solar irradiance as reference. Data for radiometric sensor calibration were acquired with the FluorSpec mounted on a tripod over grassland on the Campus of Wageningen University on April 19, 2018 (DOY 109) on a cloud-free sunny day. Measurements for the irradiance sensor calibration were acquired at 12:40 pm Central European Time (CET) for 4 min (Fig. 4a), with a tube on the top of the irradiance sensor which pointed directly at the sun. In this manuscript all time indications refer to CET. Only the raw irradiance data were used for irradiance sensor calibration.

After the irradiance optics were calibrated, the calibration was transferred to radiance optics using a white (99%) Spectralon panel. FluorSpec radiance optics were placed at 25 cm height above the horizontal reference panel (13 × 13 cm), resulting in a 5.5 cm radius FOV (Fig. 4b). Spectral data were collected at 12:50 and lasted 3 min with the irradiance sensor pointing directly up towards the sky and the radiance sensor pointing to the panel in nadir.

To assess the calibration accuracy, FluorSpec measurements were acquired over bare soil on February 27, 2019 (DOY 58) for a cloudless condition. Data were collected at 13:01, 13:11 and 13:18 for 2 min and approximately 30 measurements were acquired every time.

3.3. Ground measurements

3.3.1. FluorSpec measurements

Spectra over the potato canopy on July 23, 2018 (DOY 204) and the sugar beet canopy on August 6, 2018 (DOY 218) were measured over the full day. FluorSpec was installed at a fixed position 50 cm above the canopies, resulting in a footprint of 22 cm. FluorSpec was kept stationary acquiring measurements from nadir during the measuring day. The measurements of potato and sugar beet plants started at approximately the same time (8:28 and 8:16, respectively) and both finished at 17:06. Raw spectral data, including irradiance, dark current and radiance successively, were collected about every 25 min. Specifically, the time interval in the morning was 20 min and in the afternoon was 30 min. Each observation lasted 2–3 min and had 30–50 data records.

3.3.2. FluorPen measurements

The PAR-FluorPen FP 110/D (PSI, Czech), hereinafter called FluorPen, was used to obtain simultaneous measurements of variables related to ChF. The FluorPen is a portable, battery-powered Pulse

Fig. 3. Location of the study site 1 at Unifarm of Wageningen University, Wageningen, the Netherlands. For each flight, there were 4 flight lines in a potato field (L_1, L_2, L_3, and L_4) and 4 flight lines in a sugar beet field (L_5, L_6, L_7, and L_8). The arrows indicate the UAV flying directions over the fields.

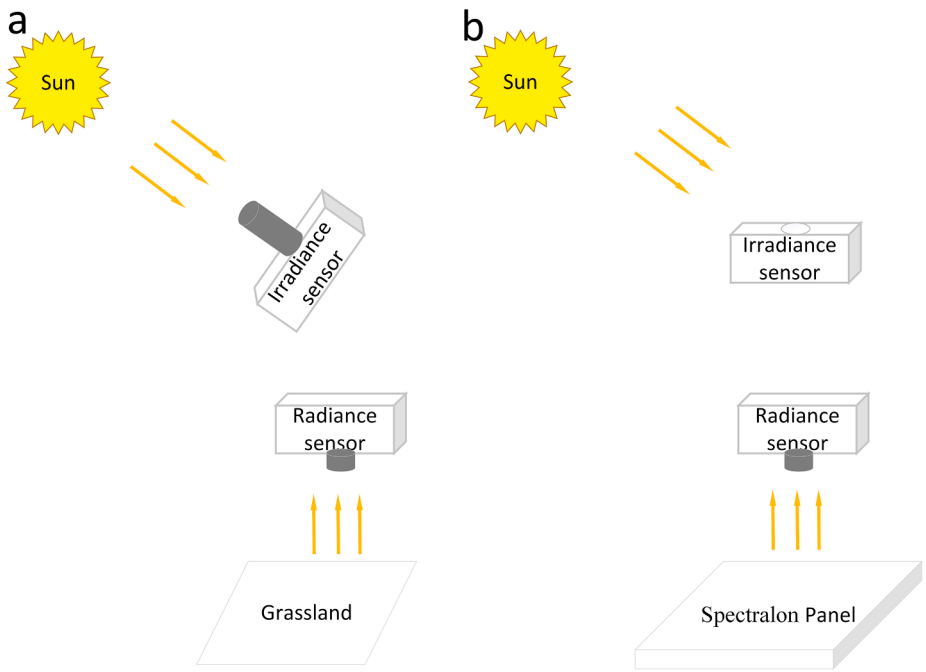

Fig. 4. The schematic diagrams of (a) irradiance sensor calibration, and (b) radiance sensor calibration. Spectra for the irradiance sensor calibration were acquired with a tube on the top of the irradiance sensor pointing directly to the sun. Data for the radiance sensor calibration were acquired over a white (99%) Spectralon panel in nadir.

amplitude-modulated fluorometer with leaf clips that enables quick and precise measurement of chlorophyll fluorescence parameters and incoming photosynthetically active radiation (PAR, μmol m^{-2} s^{-1}). Photosystem II Quantum Yield (Qy) and PAR were measured simultaneously while FluorSpec was collecting spectra diurnally. Three fully expanded young leaves from plants 30 cm away from the FOV of FluorSpec were randomly selected for the light adapted Qy measurements. The FluorPen was placed horizontally to measure the incident PAR three times per FluorSpec measurement interval.

3.4. UAV measurements

The FluorSpec was flown as a payload on a UAV over the study site 1 during clear sky conditions on August 2, 2018 (DOY 214). On that day, the maximum air temperature was 31 °C around 14:00 and the average wind speed was 2.48 m s^{-1}. Sunrise was at 6:00, solar noon at 13:43 and sunset at 21:26. The FluorSpec was mounted below a DJI S1000 UAV platform (DJI, China, Fig. 5), which is powered by 8 brushless electric rotors that allow autonomous vertical take-off and landing, hovering over a target and high manoeuvre ability during in-flight operations. Flight missions were planned with a UGCS ground station, a dedicated mission planning software that matches user observation requirements and platform/payload technical parameters (i.e., flight altitude, flight speed, sampled areas, overlapping, etc). The flight mission consisted of 27 waypoints over the two fields (Fig. 3). The UAV was programmed to fly 15 m AGL with a horizontal speed of 3 m s^{-1} from waypoint to waypoint. In this configuration, the spectrometer sampled a circular area with a diameter of 6.6 m on the ground for every measurement and the sampling interval was 10.5 m. To follow the diurnal cycle, four flights following a diurnal cycle were carried out at 9:45, 11:38, 14:15

Fig. 5. DJI S1000 octocopter UAV platform with the FluorSpec mounted. "A" refers to the FluorSpec irradiance sensor and "B" refers to the radiance sensor.

and 16:28. Each flight lasted around 12 min under clear blue sky and stable light conditions. The acquired data were processed according to the processing steps described in Section 2.3.

A Parrot Sequoia + was mounted to the DJI Mavic drone (DJI, China) to collect multispectral measurements over the two crop fields around 11:00 on the same day (DOY 214). The Parrot Sequoia + is a multispectral camera with green, red, red-edge and near-infrared (NIR) bands. The flight height was 60 m AGL and the flying speed was 5 m s^{-1}. Data processing was done using the Pix4D software, including photo alignment, digital surface model building, orthomosaic creation and calculation of the normalized difference vegetation index (NDVI).

4. Results

4.1. Radiometric and spectral characterization of the FluorSpec

The calibration result over the Spectralon panel is shown in Fig. 6a. The irradiance curve had the same trend as the radiance curve, and their difference in magnitude is almost constant over the 630–800 nm range. There were four ranges where this difference varied: 654–659 nm, 686–697 nm, 717–734 nm, and 758–770 nm. The difference between the irradiance and radiance curves was smallest at 760 nm (O_2-A absorption feature), followed by 687 nm (O_2-B absorption feature). The panel reflectance was nearly 1.0 within the 630–800 nm range. Some spectral bands showed a large noise level, especially within 717–734 nm and 758–770 nm. Even though the reflectance was evenly distributed around 1.0, the peak reached 1.2 while the lowest value was approximately 0.9 in the range of 758–770 nm.

Similarly, the spectral shape of bare soil radiance was analogous to that of irradiance (Fig. 6b). However, the difference between them became slightly smaller as wavelength increased from the red to the NIR range, because bare soil reflectance increased gradually from 0.24 at 630 nm to 0.34 at 800 nm. The irradiance acquired over the Spectralon panel was higher than that over bare soil because of different acquisition dates (12:50 on April 19, 2018, and 13:11 on February 27, 2019, respectively).

4.2. SIF retrievals in the O_2-A band from a non-vegetation target

In this paper, we only report SIF at 760 nm (O_2-A band) that corresponds to fluorescence emission in the far-red region because in the wider O_2-A absorption band this fluorescence flux is easier to quantify than in the O_2-B absorption band. To assess the ability of SSA-FLD to retrieve SIF, SIF of bare soil was calculated from collected raw FluorSpec data. SIF values were all close to zero, but slightly negative (Table 1). Vegetation SIF values usually fall in a range of $-0.15 \sim 3$ $mWm^{-2}sr^{-1}nm^{-1}$ (Rascher et al., 2015; Garzonio et al., 2017).

Table 1
Overview of the descriptive statistics of bare soil SIF values measured on February 27, 2019 (mWm^{-2} sr^{-1} nm^{-1}).

Measuring time	Maximum	Minimum	Mean	Standard deviation
13:01	−0.009	−0.110	−0.056	0.0212
13:11	−0.009	−0.086	−0.053	0.0181
13:18	−0.022	−0.088	−0.050	0.0193

4.3. Diurnal SIF and normalized SIF patterns at the ground level

4.3.1. FluorPen PAR and FluorSpec PAR

FluorSpec PAR (Wm^{-2}) was calculated within the 630–700 nm interval from the diurnal canopy FluorSpec measurements of potato on July 23, 2018, and of sugar beets on August 06, 2018. FluorPen PAR ($\mu molm^{-2}$ s^{-1}) was measured over the whole 400–700 nm interval simultaneously with the diurnal FluorSpec measurements. Fig. 7 shows the comparison between averaged FluorSpec PAR and averaged FluorPen PAR. During the two experimental days, FluorPen PAR and

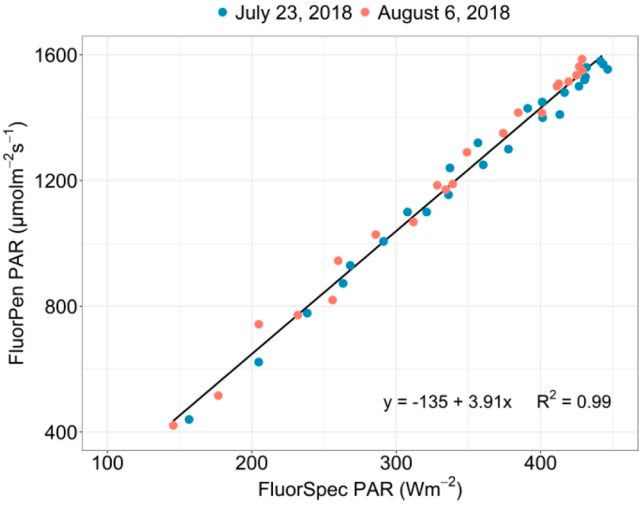

Fig. 7. The linear relations between FluorSpec PAR (Wm^{-2}) and Fluorpen PAR ($\mu molm^{-2}$ s^{-1}) for potato on July 23, 2018 (DOY 2014) (green dots) and for sugar beet on August 06, 2018 (DOY 218) (red dots). (For interpretation of the references to colour in this figure legend, the reader is referred to the web version of this article.)

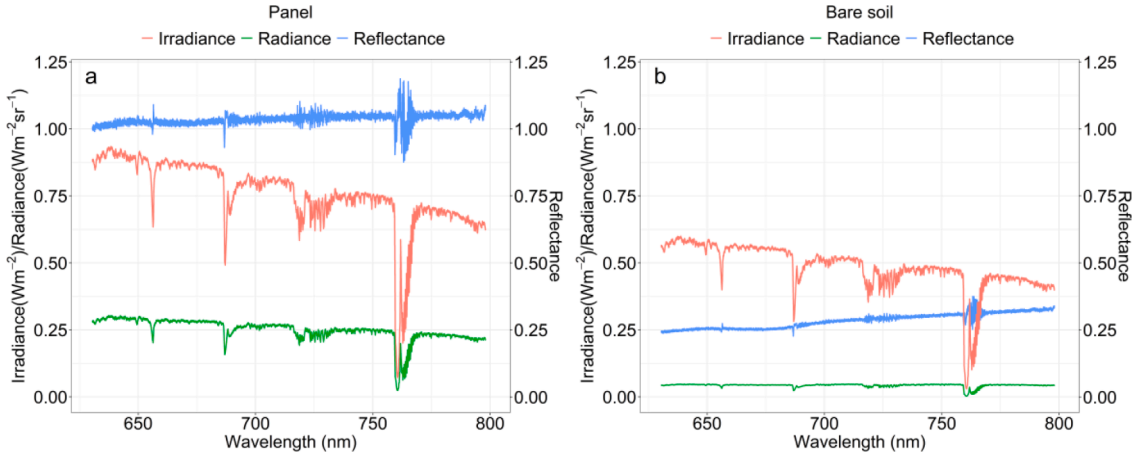

Fig. 6. Calibrated irradiance (Wm^{-2}), radiance (Wm^{-2} sr^{-1}) and reflectance over a white (99%) Spectralon panel on April 19, 2018 (a) and a bare soil sample on February 27, 2019 (b).

FluorSpec PAR had a strong linear relation, with high R^2 (0.99). Therefore, it can be concluded that incident PAR can be calculated with FluorSpec irradiance measurements within the 630–700 nm range to normalize SIF. Therefore, E_{PAR} used to normalize SIF was calculated as:

$$E_{PAR} = \left(3.91 * PAR_{FluorSpec} - 135\right)/4.56 \quad (13)$$

Division by a factor of 4.56 (Sager and McFarlane, 1997) was used to convert the FluorPen unit of E_{PAR} into Wm^{-2}.

4.3.2. Diurnal SIF cycles

The spectral and radiometric characteristics of the FluorSpec system (Fig. 6) and the good performance of SSA-FLD (Table 1) allow the quantification of SIF at 760 nm. Fig. 8 shows the diurnal cycles of SIF values of potato and sugar beet canopies, which were measured at regular intervals on July 23, 2018 and August 06, 2018, respectively. SIF exhibited a pronounced diurnal pattern with the highest average values measured close to midday. Potato SIF increased quickly till it reached the highest value around 12:30, and in the afternoon potato SIF experienced a sharp decline (Fig. 8a). In comparison, in Fig. 8b, SIF values of the sugar beet crop increased slowly until approximately 12:30. Interestingly, sugar beet SIF decreased gradually in the early afternoon unlike potato, but afterwards it went down steeply (Fig. 8b). Both the range and the variations in SIF of potato were larger than those of sugar beets, despite their similar SIF diurnal patterns. PAR from FluorSpec on both days had clear diurnal patterns. PAR increased in the morning and peaked around local noon (around 13:30 pm) (Fig. 8). Afterwards, PAR decreased. For both crops, the peaks of SIF values appeared earlier than those of PAR.

4.3.3. Diurnal normalized SIF

The normalized SIF was calculated at 760 nm with PAR, which was calculated using the FluorSpec PAR-based linear model that was introduced in Section 4.3.1 (Fig. 7). The diurnal changes of $SIF_{normalized}$ are shown in Fig. 9a, b. The graphs show that there was a steady decrease in $SIF_{normalized}$ values of both crops during the day. Overall, $SIF_{normalized}$ values of potatoes were lower than those of sugar beets. FluorPen Qy was compared to assess the reliability of $SIF_{normalized}$ (Fig. 10a, b). Qy indicates the quantum yield of linear electron flux through the Photosystem II (PSII) reaction centres, which can be used to represent the PSII operating efficiency under different environmental conditions (Baker, 2008). In this study, FluorPen Qy was measured in light-adapted leaf samples. Both potato and sugar beet crops showed significant positive correlations between $SIF_{normalized}$ and Qy in Fig. 10. Potatoes had a higher correlation than sugar beets, with R^2 values of 0.81 and 0.63, respectively.

4.4. Diurnal dynamics of UAV-based SIF

Maps of SIF acquired from the UAV platform over the two selected crop fields clearly show novel information on plant structure and function (Fig. 11). SIF performed differently in different fields at the same time. For instance, at 11:38, SIF in the potato field (towards the south) changed over a larger range from 0.23 to 1.42 $mWm^{-2}sr^{-1}nm^{-1}$, while for sugar beets (towards the north) it varied from 0.51 to 1.34 $mWm^{-2}\,sr^{-1}nm^{-1}$. Some areas had fluorescence values close to zero, e.g. the senescent potato areas covered by the 4th flight line (L_4 in Fig. 11). The lower SIF (blue points) was consistent with low NDVI values in the potato field (particularly the headlands). Large variation could be observed within the same field. For the 2nd flight at 11:38, SIF from different flight lines shows clear variations either in potato or sugar beet fields. In the potato field, L_1 has consistently the highest fluorescence values reaching 1.42 $mWm^{-2}\,sr^{-1}\,nm^{-1}$, whereas the maximum value of L_2 was 1.05 $mWm^{-2}\,sr^{-1}\,nm^{-1}$ (Fig. 11). Furthermore, SIF was observed to be highly variable within the same flight line. For example, L_2 of the 2nd flight within the potato field ranged from 0.35 to 1.06 $mWm^{-2}\,sr^{-1}\,nm^{-1}$.

Clear diurnal cycles of SIF in the two fields were shown by comparing the four maps over the day. The overall SIF went up in the morning and went down in the afternoon, which is in line with SIF diurnal cycles at the canopy level (Fig. 8). SIF values at 9:44 and at 16:28 were lower than those at 11:38 and 14:45. SIF performed similarly in the 2nd and 3rd flights as their observing times were both close to solar noon when the incoming radiation was highest. This is different from the diurnal performance of potato SIF at the ground level, where SIF around 11:40 was higher than that around 14:00.

5. Discussion

This study introduced a UAV-based fluorescence measuring system, FluorSpec, whose measurements can be used as a proxy for crop photosynthesis and stress occurring in crops both at the ground and the field level. Some earlier studies have shown the potential of UAV mounted systems to measure SIF with a non-imaging spectrometer (Bendig et al., 2019; Garzonio et al., 2017; MacArthur et al., 2014). Compared with these studies, the current study has two advantages. First, the FluorSpec FOV is 25°, which is larger than that of the systems used in the above-mentioned literature (largest FOV of 15°). Optionally, FluorSpec can be mounted with fore optics, reducing the FOV to any narrower opening angle. As Gautam et al. (2018) pointed out, increasing the FOV can compensate the footprint area loss and increase the signal strength. Thus, the 25° FOV provides stable and reliable signals. No

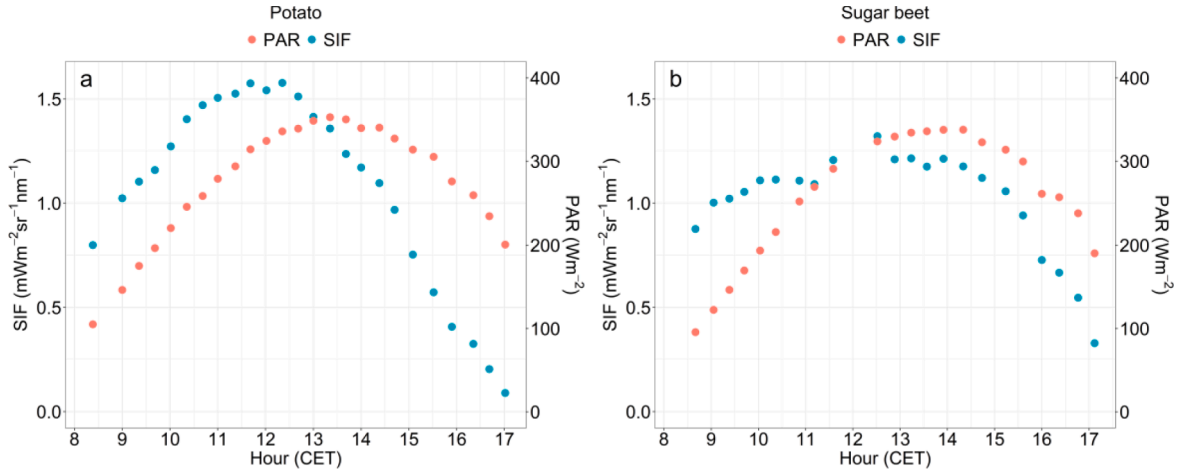

Fig. 8. Diurnal dynamics of SIF and PAR for potato on July 23, 2018 (DOY 204) (a) and for sugar beet on August 06, 2018 (DOY 218) (b). Each value represents mean SIF and mean PAR values collected at this time.

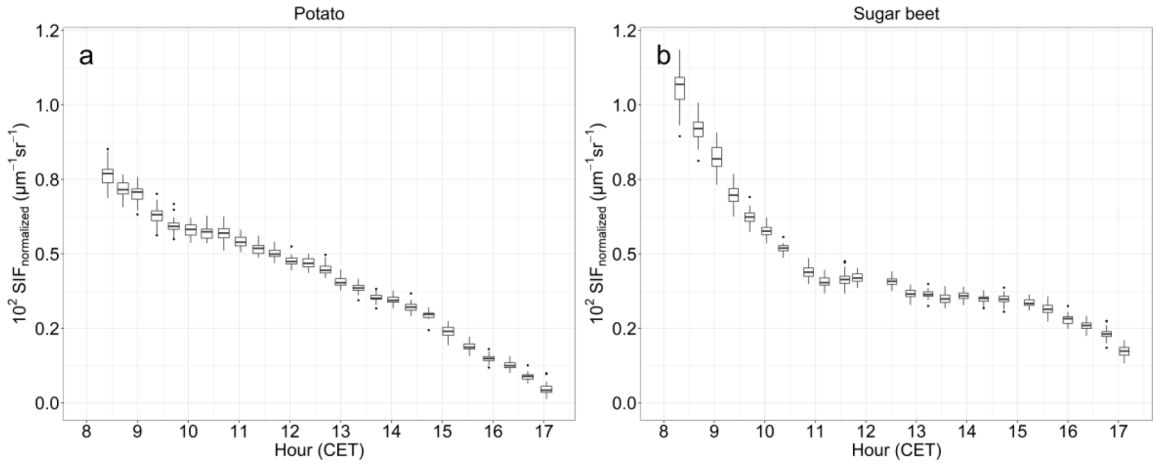

Fig. 9. Diurnal patterns of the normalized SIF by E_{PAR} ($SIF_{normalized}$) over potatoes (a) and sugar beets (b). $SIF_{normalized}$ values were multiplied by 100. Each box with whiskers represents all $SIF_{normalized}$ calculated using SIF values acquired during the measuring time.

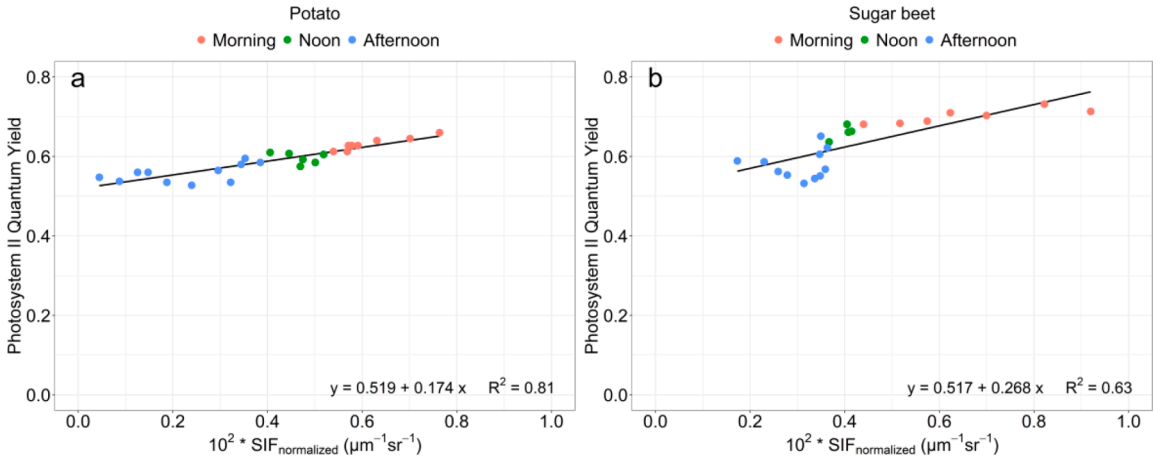

Fig. 10. Relationships between averaged normalized SIF ($SIF_{normalized}$) and FluorPen Photosystem II Quantum Yield (Qy) for potatoes (a) and for sugar beets (b). $SIF_{normalized}$ values were multiplied by 100.

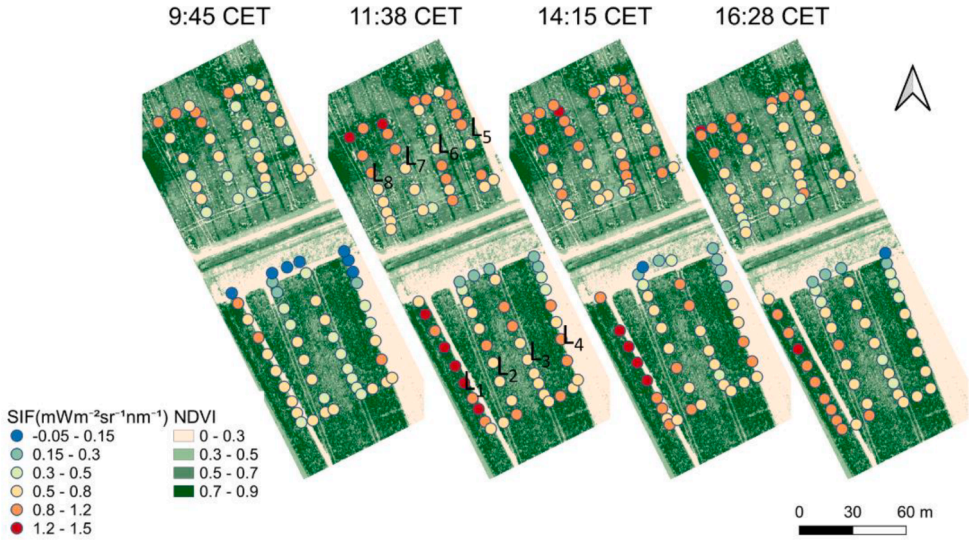

Fig. 11. Performance of SIF in potato and sugar beet fields based on UAV measurements as obtained on August 02, 2018 (DOY 214) over the experimental area in Wageningen, the Netherlands. L_1, L_2, L_3, and L_4 were flight lines over the potato field and L_5, L_6, L_7, and L_8 were over the sugar beet field. The basemap shows NDVI values derived from a Sequoia + multi-spectral image.

matter what flight mode is applied, e.g., stop and go (hovering) or continuous mapping, FluorSpec SIF signals can provide a better understanding of crop photosynthetic performance due to the larger footprint. In our study, the continuous mapping flight mode was applied and enabled us to have more insights into SIF performance of larger areas within and between fields. Secondly, the atmosphere between the sensor and target affects airborne SIF retrieval (Damm et al., 2014) and adds uncertainties in SIF observations even at short distances of 10 m such as tower and UAV observations (Sabater et al., 2018). In our study, atmospheric correction was applied to FluorSpec measurements, which increases the reliability of the SIF retrieval.

5.1. The performances of radiometric correction and SSA-FLD

The white Spectralon panel and bare soil show the expected spectral behaviour after radiometric calibration and atmospheric correction (Fig. 6a, b). In the spectral range from 630 to 800 nm, the reflectance of the white panel was constant while the reflectance of bare soil increased from 0.24 to 0.34. This demonstrates that the FluorSpec system was well calibrated and provided realistic reflectance values at very high spectral resolution. SIF of bare soil shows very small negative values close to zero (Table 1), indicating no fluorescence as should be. The negative SIF values from non-vegetation targets have also been observed in other studies (Alonso et al., 2008; Damm et al., 2014; Garzonio et al., 2017; Pinto et al., 2016). For example, Alonso et al. (2008) found that SIF values retrieved from bare soil by the iFLD method, one of the most popular methods to provide reasonable fluorescence values, were also negative and most of them varied from −0.25–0 $mWm^{-2}\ sr^{-1}\ nm^{-1}$. Negative SIF values could result from the combined effects of sensor noise and the retrieval assumption of a known shape of the fluorescence spectrum over vegetation, whereas this assumption is not suitable for non-vegetation targets (bare soil). The similar performance of SSA-FLD shows its capability to separate SIF from reflectance.

In the future, the measured SIF values over canopies as obtained with FluorSpec need to be validated by comparing them with a well-calibrated system like the airborne HyPlant system as a reference. A special campaign has been defined for this.

5.2. Diurnal cycles of ground-based SIF and $SIF_{normalized}$

Our results are in agreement with findings of previous studies (Rascher et al., 2015; Zarco-Tejada et al., 2016): (i) crop SIF values are in the range of 0 to 3 $mW\ m^{-2}\ sr^{-1}\ nm^{-1}$, both at the ground level and at the UAV level; (ii) SIF increased in the morning and decreased in the afternoon, which is mainly driven by PAR. As illustrated, for both potato and sugar beet crops, the peak of SIF occurred about an hour earlier than that of PAR (Fig. 8). There are three possible explanations for this. One explanation is that the incoming irradiance was high around 12:30 and light energy absorption already might have exceeded the capacity for light utilization in photosynthesis, in which case photoinhibition would be triggered. Excess of absorbed light energy was dissipated into heat by nonphotochemical chlorophyll fluorescence quenching (NPQ), which is the primary mechanism to dissipate the absorbed energy when light intensity is high. Secondly, the summer of 2018 brought a heatwave to the Netherlands, therefore there was increased heat stress and drought. The maximum temperatures were 30 °C and 32 °C on July 23, 2018 (DOY 204) and August 6, 2018 (DOY 218), respectively. The enzymes of the Calvin cycle involved in the carbon assimilation system are heat labile. For example, Rubisco activase, which affects Rubisco activity, is very sensitive to the elevated temperature. Thus, the carbon fixation process is sensitive to elevated temperature and gets strongly inhibited by heat stress (Berry and Bjorkman 1980). In addition, stressed by drought, the crops had to close leaf stomata to prevent water vapor loss. Since stomata act as a gateway for water and CO_2, their closure limits the transport of CO_2 into leaves for use in carbon fixation and consequently affects the electron transport chain in light-dependent reactions. As a result, most incoming sunlight could not be processed in photochemical ways and was emitted as heat. To further reduce water vapor loss, crop leaves wilted, and PAR absorption decreased. The energy used to emit fluorescence was out of sync with incoming irradiance acquired by the FluorSpec upward sensor. Another possible reason could be the short sensor-target distance. The FluorSpec was positioned 50 cm above both crop canopies and as a result covered a 22 cm-diameter circular area. The close distance could have made the SIF signal vulnerable to the solar zenith angle and BRDF effects. The small footprint also only allowed SIF acquisition over a limited canopy area, which could be affected by leaf inclination angle, canopy structure, soil background, and the plant shadow caused by the direct sunlight around solar noon.

In this study, PAR from the FluorPen is not ideal for SIF normalization for the following two reasons. Firstly, the starting time of the FluorSpec and PAR FluorPen measurements is slightly different, resulting in differences between the acquired incoming irradiance. Secondly, FluorPen measurements may not be always available due to the experimental purposes and set-ups, for example, when many other parameters need to be acquired at the same time with FluorPen. Therefore, FluorSpec data was used to model FluorPen PAR using the equation in Fig. 7. For both crops, $SIF_{normalized}$ decreased during the measuring period (Fig. 9). At the middle of the morning, although the ChF emission increases with PAR (Fig. 8), normalized SIF strongly decreased because the stressed plant was not able to cope with the increasing light intensity. This decrease indicates that most of the incoming sunlight was not used for photosynthesis, which is consistent with observations in other work (Amoros-Lopez et al., 2008; Xu et al., 2018). According to Amoros-Lopez et al. (2008), in their study the fluorescence yield rose again in the late evening after 17:00, matching the decrease in the light intensity. In our study, the field experiments ended around 17:00 when the plants were still suffering from the heat wave and NPQ remained active. Although having similar declining trends, normalized SIF values of potatoes were lower than those of sugar beets. This could be caused by the different canopy structure (e.g., leaf angles and leaf size), physiological factors (different growth stages), or the combination of these or more factors. Since SIF represents a small amount of the radiance measured by the sensor, small differences in these factors can result in different performances of SIF and SIF normalization. Further research is needed to determine main reasons. The Photosystem II Quantum Yield (Qy) measured with the Fluorpen was used to validate the normalized SIF. The resulting high R^2 (0.81 for potatoes and 0.63 for sugar beets, Fig. 10) for the relationship between Qy and $SIF_{normalized}$ shows that SIF normalized by PAR modeled from FluorSpec irradiance is a good indicator of crop photosynthesis. For sugar beets, the relationship between $SIF_{normalized}$ and Qy from 14:00 and 16:00 was seriously off and under the regression line (Fig. 10). One possible explanation could be that the physiological response to the high light intensity and drought stress at the leaf level is different for different crops. For example, in the early afternoon, leaves of stressed sugar beet plants wilted more obviously than the stressed potato leaves. In addition, compared with potato plants, there were fewer sugar beet leaves in the FluorSpec footprint due to the larger size of sugar beet leaves. The FluorSpec captured SIF from fewer individual leaves compared to potato, which were less representative for the canopy SIF.

5.3. Diurnal cycles of UAV-based SIF

The value range and the diurnal cycle of UAV-based SIF proves the feasibility of the FluorSpec system to acquire SIF at the field level. The value range of FluorSpec SIF in the O_2-A band (Fig. 11) is in a strong agreement with those from other UAV-based and airborne systems, which varies between 0 and 3 $mWm^{-2}\ sr^{-1}\ nm^{-1}$ depending on the characteristics of different target surfaces (Bendig et al., 2019; Garzonio et al., 2017; Rascher et al., 2015). Like SIF at the ground level, SIF derived from a UAV platform showed clear diurnal patterns both in a potato field and a sugar beet field. This further confirms the ability of a

UAV platform to capture SIF changes diurnally at a low attitude. However, at the field level, potato SIF values from the 1st flight at 11:38 were slightly higher but close to those from the 3rd flight at 14:15, which was different from potato SIF changes at the ground level. This mismatch could be caused by the spatial scales. This is because that, at the ground level, the canopy structure within in the FluorSpec footprint, the solar zenith angle and the BRDF effect had a stronger influence on SIF values and its changes.

SIF of potato plants varied more than that of sugar beets (Fig. 11). This could be a physiological difference, because the two crops were at different growing stages. Sugar beet was still growing in the 2018 survey period and had a dense fully mature canopy in late summer 2018. However, potatoes already approached senescence during the time of observation (beginning of August 2018). Despite the still green leaf material and a dense vegetation cover, the growing conditions of potato plants were less uniform compared to the sugar beet plants.

5.4. Limitations at the UAV level

Although the UAV-based FluorSpec system can capture the SIF signal and bridge the spatial gap with airborne SIF, some aspects of the study remain challenging. First, accurately geolocating the footprint of FluorSpec measurements is a challenge. This is a common problem for UAV-based point observations. An example is the study of MacArthur et al. (2014), in which their UAV platform not only lacked positioning and orientation of sensors but also the associated geometric processing workflow for an accurate ground projection of the spectroradiometer's FOV. UAV movements like pitch and roll caused variations of the footprint areas sampled by the non-imaging spectrometer at the ground (Garzonio et al., 2017). Similarly, Bendig et al. (2019) pointed out that it is challenging to obtain the weak SIF signal from a UAV-based QE-Pro spectrometer. In their study, the footprints between repetitive UAV flights spatially misaligned, which was also the case in our study. From Fig. 11 we can see that flight lines did not always overlap perfectly and there was a recognizable spatial variation in the SIF values. One reason is that the flights were conducted without gimbal mounted to the UAV. The movements of the UAV (roll, yaw, and pitch) change the pointing directions of the two optics, resulting in non-nadir point observations. Also, the absence of an inertial measurement unit (IMU) made it less feasible to correct drone movements. The GPS sensors both on the drone and the FluorSpec sensor were not free of positioning errors, and thereby increased the uncertainty of the measurement locations.

In addition, the lean of the system caused by the UAV in-flight movements would also influence the downwelling irradiance measurements (Bendig et al., 2018, 2019), since the irradiance cosine corrector was not mounted on a gimbal. According to Bendig et al. (2019), when the flying speed is 2–3 m s^{-1} or even lower in low wind conditions (<5.6 m s^{-1}), there is less need for motion correction. In our case, the flying speed was 3 m s^{-1} and the wind speed during the flights was less than 5.3 m s^{-1}. Therefore, in this study we ignored the influence from the system tilt on the irradiance. To address this problem in future studies, irradiance measurements taken before and after the flights can be averaged to replace the in-flight irradiance, since the flights are conducted under clear sky weather conditions. Alternatively, on a windless day, the tilting can average out over all the flight lines, and in that case the average of all irradiance spectra over the whole flight can be used.

Another drawback is that no validation data for the UAV-based SIF were available. We only have one QE-pro spectrometer and it was not feasible to collect ground-based and UAV-based field level SIF measurements at the same time or immediately after the flights as four flights were carried out within a day. As stated before, the UAV-based SIF values over canopies will be validated in a follow-up study by comparing it with a well-calibrated reference system, like the airborne HyPlant system.

5.5. Ways to improve the data quality of the UAV-based FluorSpec

This point-measuring UAV spectroscopy system can be improved in three aspects. First, a good flight mission plays a key role in improving SIF retrieval accuracy by acquiring high-quality data. Thus, the inputs into the ground station, such as the flight height and flight speed, should be carefully considered while designing the flight mission. For example, Garzonio et al. (2017) found that the lower flying altitude (10 m AGL) allows retrieving fluorescence in absolute units and a high-flying UAV setup (20 m AGL) enables the radiometric signal sampled during repeated measurements to be less subject to small changes of the platform location, roll and pitch angles. The decision of feasible flying parameters should take the scientific question and objective into account. Secondly, pairing the FluorSpec with a Real-Time Kinematic (RTK) enabled GNSS IMU device and installing the system on a stabilized gimbal could potentially improve the georectification accuracy down to centimetre-level positioning. Thirdly, a co-registered RGB camera can help to identify the footprint centre of the point measurements. RGB images can be processed by the Structure from Motion (SfM) algorithm (Westoby et al., 2012), which enables the reconstruction of the UAV orientation information (pitch and roll angles). RGB images can also support a visual identification of targets within the footprints and improve the understanding of SIF performance.

5.6. Suggestions on improving SIF comparison with other studies

Technical advantages of UAVs include the capability for highly customized deployments, quick response and turn-around for planning and investigation (Mohammed et al., 2019). Currently, more efforts are being invested in this research topic. For different UAV-based fluorescence measuring systems, protocols to acquire good and comparable measurements are necessary. This would allow testing different systems, combining data from different sensors (e.g., AirSIF, FluorSpec and HyUAS), and comparing SIF observations from different spatial scales with airborne SIF. According to our knowledge, some points can be added to the protocols. First, good and similar weather conditions are key to compare SIF values, since the SIF signal is weak and vulnerable to weather changes. Secondly, SIF is highly dynamic and sensitive, and thus a similar take-off time increases the reliability of the comparison. For instance, solar noon is a good time, as it can reduce the impact of solar angles. Thirdly, the flight pattern is also important. The two main flight modes are a hovering pattern and a continuous flying pattern. To obtain reliable data, the same flight mode should be applied all the time. In addition, a well-equipped UAV-based SIF measuring system is needed for an accurate geo-location of SIF measurements, e.g., with a gimbal and an IMU installed if possible.

6. Conclusions

This study demonstrated the system set-up and the processing chain of a novel UAV-based system, FluorSpec, to measure SIF at the O_2-A band for different crops at a low flying altitude. FluorSpec can collect high spectral resolution data, repeatedly over time, providing strong support for novel scientific approaches in monitoring crop photosynthetic activities and growth conditions (e.g., heat stress and drought stress), for instance within the context of precision agriculture. Within this application field it can be considered a flexible, low-cost system with clear potential.

The FluorSpec can acquire reliable spectral measurements after radiometric sensor calibration. The near-zero SIF values from the non-fluorescence emitting bare soil confirmed SSA-FLD's capability of disentangling the fluorescence signal from canopy reflectance. Ground-based SIF over potato and sugar beet canopies exhibited obvious diurnal patterns, and their differences demonstrated that SIF varied depending on the crop types. These differences could also be seen in the diurnal changes of the normalized SIF, the reliability of which was

indicated by the good correlation with Qy. The fact that SIF is dominated by incoming irradiance but also influenced by other factors (e.g. heat stress) was further supported by the differences of diurnal SIF and PAR patterns and the decreasing trend of the normalized SIF. The great potential of a UAV platform to obtain SIF information at a low flying altitude and to combine this with airborne SIF products was proven by the reasonable value range of SIF at the field scale and the pronounced temporal dynamics of both studied crops. The variations shown in the same flight mainly due to the crop species, growth status and spatial heterogeneity were consistent with previous studies, which shows that the UAV-based FluorSpec system is a reliable system to measure actual SIF values.

In conclusion, the FluorSpec system, equipped with a cost-effective non-imaging instrument aboard a UAV, contributes to exploring crop SIF and photosynthetic activities in precision farming and upscaling the SIF measuring from the ground level to the field level by providing accurate, high resolution and flexible spectral measurements.

CRediT authorship contribution statement

Na Wang: Conceptualization, Data curation, Formal analysis, Methodology, Software, Visualization, Writing - original draft. **Juha Suomalainen:** Methodology, Software, Supervision, Writing - original draft, Writing - review & editing. **Harm Bartholomeus:** Data curation, Formal analysis, Methodology, Supervision, Writing - review & editing. **Lammert Kooistra:** Formal analysis, Supervision, Methodology, Writing - review & editing. **Dainius Masiliūnas:** Formal analysis, Software, Visualization, Writing - review & editing. **Jan G.P.W. Clevers:** Formal analysis, Methodology, Supervision, Writing - review & editing.

Declaration of Competing Interest

The authors declare that they have no known competing financial interests or personal relationships that could have appeared to influence the work reported in this paper.

Acknowledgements

This work of the first author (N. Wang) is supported by the China Scholarship Council (CSC) under Grant 201704910780. All authors would like to thank Marcello Novani from Wageningen University for his assistance in testing the FluorSpec system and collecting field data and Benjamin Brede from Wageningen University for his help in acquiring UAV-based FluorSpec data. We also thank Peiqi Yang from the University of Twente for his feedback on some questions about data analysis.

References

Alonso, L., Gomez-Chova, L., Vila-Frances, J., Amoros-Lopez, J., Guanter, L., Calpe, J., Moreno, J., 2008. Improved fraunhofer line discrimination method for fluorescence quantification. IEEE Geosci. Remote Sens. Lett. 5, 620–624. https://doi.org/10.1109/lgrs.2001180.

Amoros-Lopez, J., Gomez-Chova, L., Vila-Frances, J., Alonso, L., Calpe, J., Moreno, J., del Valle-Tascon, S., 2008. Evaluation of remote sensing of vegetation fluorescence by the analysis of diurnal cycles. Int. J. Remote Sens. 29, 5423–5436. https://doi.org/10.1080/01431160802036391.

Baker, N.R., 2008. Chlorophyll fluorescence: a probe of photosynthesis in vivo. Annu. Rev. Plant Bio. 59, 89–113. https://doi.org/10.1146/annurev.arplant.59.032607.092759.

Bendig, J., Gautam, D., Malenovský, Z., Lucieer, A., 2018. Influence of cosine corrector and UAS platform dynamics on airborne spectral irradiance measurements. In: IGARSS 2018–2018 IEEE International Geoscience and Remote Sensing Symposium, pp. 8822–8825. https://doi.org/10.1109/IGARSS.2018.8518864.

Bendig, J., Malenovsky, Z., Gautam, D., Lucieer, A., 2019. Solar-induced chlorophyll fluorescence measured from an Unmanned Aircraft System: Sensor etaloning and platform motion correction. IEEE Trans. Geosci. Remote Sens. 1–8 https://doi.org/10.1109/tgrs.2019.2956194.

Berry, J., Bjorkman, O., 1980. Photosynthetic response and adaptation to temperature in higher plants. Annu. Rev. Plant Physiol. 31, 491–543.

Camino, C., Gonzalez-Dugo, V., Hernandez, P., Zarco-Tejada, P.J., 2019. Radiative transfer Vcmax estimation from hyperspectral imagery and SIF retrievals to assess photosynthetic performance in rainfed and irrigated plant phenotyping trials. Remote Sens. Environ. 231, 111186 https://doi.org/10.1016/j.rse.2019.05.005.

Cheng, Y.B., Middleton, E.M., Zhang, Q., Huemmrich, K.F., Campbell, P.K., Cook, B.D., Kustas, W.P., Daughtry, C.S., 2013. Integrating solar induced fluorescence and the photochemical reflectance index for estimating gross primary production in a cornfield. Remote Sens. 5, 6857–6879. https://doi.org/10.3390/rs5126857.

Cogliati, S., Rossini, M., Julitta, T., Meroni, M., Schickling, A., Burkart, A., Pinto, F., Rascher, U., Colombo, R., 2015. Continuous and long-term measurements of reflectance and sun-induced chlorophyll fluorescence by using novel automated field spectroscopy systems. Remote Sens. Environ. 164, 270–281. https://doi.org/10.1016/j.rse.2015.03.027.

Damm, A., Elbers, J., Erler, A., Gioli, B., Hamdi, K., Hutjes, R., Kosvancova, M., Meroni, M., Miglietta, F., Moersch, A., 2010. Remote sensing of sun-induced fluorescence to improve modeling of diurnal courses of gross primary production (GPP). Glob. Change Biol. 16, 171–186. https://doi.org/10.1111/j.1365-2486.2009.01908.x.

Damm, A., Guanter, L., Laurent, V.C.E., Schaepman, M.E., Schickling, A., Rascher, U., 2014. FLD-based retrieval of sun-induced chlorophyll fluorescence from medium spectral resolution airborne spectroscopy data. Remote Sens. Environ. 147, 256–266. https://doi.org/10.1016/j.rse.2014.03.009.

Daumard, F., Champagne, S., Fournier, A., Goulas, Y., Ounis, A., Hanocq, J.-F., Moya, I., 2010. A field platform for continuous measurement of canopy fluorescence. IEEE Trans. Geosci. Remote Sens. 48, 3358–3368. https://doi.org/10.1109/TGRS.2010.2046420.

Daumard, F., Goulas, Y., Champagne, S., Fournier, A., Ounis, A., Olioso, A., Moya, I., 2012. Continuous monitoring of canopy level sun-induced chlorophyll fluorescence during the growth of a sorghum field. IEEE Trans. Geosci. Remote Sens. 50, 4292–4300. https://doi.org/10.1109/TGRS.2012.2193131.

Foley, J.A., Ramankutty, N., Brauman, K.A., Cassidy, E.S., Gerber, J.S., Johnston, M., Mueller, N.D., O'Connell, C., Ray, D.K., West, P.C., Balzer, C., Bennett, E.M., Carpenter, S.R., Hill, J., Monfreda, C., Polasky, S., Rockström, J., Sheehan, J., Siebert, S., Tilman, D., Zaks, D.P.M., 2011. Solutions for a cultivated planet. Nature 478, 337–342. https://doi.org/10.1038/nature10452.

Frankenberg, C., Fisher, J.B., Worden, J., Badgley, G., Saatchi, S.S., Lee, J.E., Toon, G.C., Butz, A., Jung, M., Kuze, A., 2011. New global observations of the terrestrial carbon cycle from GOSAT: patterns of plant fluorescence with gross primary productivity. Geophys. Res. Lett. 38 https://doi.org/10.1029/2011GL048738.

Frankenberg, C., O'Dell, C., Berry, J., Guanter, L., Joiner, J., Köhler, P., Pollock, R., Taylor, T.E., 2014. Prospects for chlorophyll fluorescence remote sensing from the Orbiting Carbon Observatory-2. Remote Sens. Environ. 147, 1–12. https://doi.org/10.1016/j.rse.2014.02.007.

Garzonio, R., Di Mauro, B., Colombo, R., Cogliati, S., 2017. Surface reflectance and sun-induced fluorescence spectroscopy measurements using a small hyperspectral UAS. Remote Sens. 9, 472. https://doi.org/10.3390/rs9050472.

Gautam, D., Watson, C., Lucieer, A., Malenovský, Z., 2018. Error budget for geolocation of spectroradiometer point observations from an unmanned aircraft system. Sensors 18 (10), 3465.

Goulas, Y., Fournier, A., Daumard, F., Champagne, S., Ounis, A., Marloie, O., Moya, I., 2017. Gross primary production of a wheat canopy relates stronger to far red than to red solar-induced chlorophyll fluorescence. Remote Sens. 9, 97. https://doi.org/10.3390/rs9010097.

Guan, K., Berry, J.A., Zhang, Y., Joiner, J., Guanter, L., Badgley, G., Lobell, D.B., 2016. Improving the monitoring of crop productivity using spaceborne solar-induced fluorescence. Glob. Change Biol. 22, 716–726. https://doi.org/10.1111/gcb.13136.

Guanter, L., Aben, I., Tol, P., Krijger, J., Hollstein, A., Köhler, P., Damm, A., Joiner, J., Frankenberg, C., Landgraf, J., 2015. Potential of the TROPOspheric Monitoring instrument (TROPOMI) onboard the Sentinel-5 Precursor for the monitoring of terrestrial chlorophyll fluorescence. Atmos. Meas. Tech. 8, 1337–1352. https://doi.org/10.5194/amt-8-1337-2015.

Guanter, L., Zhang, Y., Jung, M., Joiner, J., Voigt, M., Berry, J.A., Frankenberg, C., Huete, A.R., Zarco-Tejada, P., Lee, J.-E., Moran, M.S., Ponce-Campos, G., Beer, C., Camps-Valls, G., Buchmann, N., Gianelle, D., Klumpp, K., Cescatti, A., Baker, J.M., Griffis, T.J., 2014. Global and time-resolved monitoring of crop photosynthesis with chlorophyll fluorescence. Proc. Natl. Acad. Sci. 111, E1327–E1333. https://doi.org/10.1073/pnas.1320008111.

James, A., Plascyk, J., 1975. The MK II fraunhofer line discriminator (FLD-II) for airborne and orbital remote sensing of solar-stimulated luminescence. Opt. Eng. 14 (4), 144339 https://doi.org/10.1117/12.7971842.

Joiner, J., Guanter, L., Lindstrot, R., Voigt, M., Vasilkov, A., Middleton, E., Huemmrich, K., Yoshida, Y., Frankenberg, C., 2013. Global monitoring of terrestrial chlorophyll fluorescence from moderate spectral resolution near-infrared satellite measurements: methodology, simulations, and application to GOME-2. Atmos. Meas. Tech. 6, 2803–2823. https://doi.org/10.5194/amt-6-2803-2013.

Kalaji, H.M., Jajoo, A., Oukarroum, A., Brestic, M., Zivcak, M., Samborska, I.A., Cetner, M.D., Łukasik, I., Goltsev, V., Ladle, R.J., 2016. Chlorophyll a fluorescence as a tool to monitor physiological status of plants under abiotic stress conditions. Acta Physiologiae Plantarum. 38, 102. https://doi.org/10.1007/s11738-016-2113-y.

Kalaji, M.H., Goltsev, V.N., Żuk-Gołaszewska, K., Zivcak, M., Brestic, M., 2017. Chlorophyll fluorescence: Understanding crop performance — basics and applications, 1 ed. CRC Press, Florida.

Li, Z., Zhang, Q., Li, J., Yang, X., Wu, Y., Zhang, Z., Wang, S., Wang, H., Zhang, Y., 2020. Solar-induced chlorophyll fluorescence and its link to canopy photosynthesis in maize from continuous ground measurements. Remote Sens. Environ. 236, 111420 https://doi.org/10.1016/j.rse.2019.111420.

MacArthur, A., Robinson, I., 2015. A critique of field spectroscopy and the challenges and opportunities it presents for remote sensing for agriculture, ecosystems, and hydrology. Int. Soc. Opt. Photonics 9637, 963705. https://doi.org/10.1117/12.2201046.

MacArthur, A., Robinson, I., Rossini, M., Davis, N., MacDonald, K., 2014. A dual-field-of-view spectrometer system for reflectance and fluorescence measurements (Piccolo Doppio) and correction of etaloning. In: Proceedings of the 5th International Workshop on Remote Sensing of Vegetation Fluorescence, pp. 22–24.

Maier, S.W., Günther, K.P., Stellmes, M., 2004. Sun-induced fluorescence: a new tool for precision farming. Dig. Imaging Spectral Tech.: Appl. Precis. Agric. Crop Physiol. 66, 207–222. https://doi.org/10.2134/asaspecpub66.c16.

Maseyk, K., Atherton, J., Thomas, R.M., Wood, K., Tausz-Sabine, S., Mac Arthur, A., Porcar-Castell, A., Tausz, M., 2018. UAV-based measurements of solar induced fluorescence to gain insight into canopy-level photosynthesis under elevated CO_2. AGU Fall Meeting Abstracts.

Mazzoni, M., Meroni, M., Fortunato, C., Colombo, R., Verhoef, W., 2012. Retrieval of maize canopy fluorescence and reflectance by spectral fitting in the O_2–A absorption band. Remote Sens. Environ. 124, 72–82. https://doi.org/10.1016/j.rse.2012.04.025.

Meroni, M., Barducci, A., Cogliati, S., Castagnoli, F., Rossini, M., Busetto, L., Migliavacca, M., Cremonese, E., Galvagno, M., Colombo, R., 2011. The hyperspectral irradiometer, a new instrument for long-term and unattended field spectroscopy measurements. Rev. Sci. Instrum. 82, 043106 https://doi.org/10.1063/1.3574360.

Meroni, M., Busetto, L., Colombo, R., Guanter, L., Moreno, J., Verhoef, W., 2010. Performance of spectral fitting methods for vegetation fluorescence quantification. Remote Sens. Environ. 114, 363–374. https://doi.org/10.1016/j.rse.2009.09.010.

Mohammed, G.H., Colombo, R., Middleton, E.M., Rascher, U., van der Tol, C., Nedbal, L., Goulas, Y., Pérez-Priego, O., Damm, A., Meroni, M., 2019. Remote sensing of solar-induced chlorophyll fluorescence (SIF) in vegetation: 50 years of progress. Remote Sensing of Environment. 231 https://doi.org/10.1016/j.rse.2019.04.030.

Moya, I., Camenen, L., Evain, S., Goulas, Y., Cerovic, Z., Latouche, G., Flexas, J., Ounis, A., 2004. A new instrument for passive remote sensing: 1. Measurements of sunlight-induced chlorophyll fluorescence. Remote Sens. Environ. 91 (2), 186–197. https://doi.org/10.1016/j.rse.2004.02.012.

Pinto, F., Damm, A., Schickling, A., Panigada, C., Cogliati, S., Müller-Linow, M., Balvora, A., Rascher, U., 2016. Sun-induced chlorophyll fluorescence from high-resolution imaging spectroscopy data to quantify spatio-temporal patterns of photosynthetic function in crop canopies. Plant, Cell Environ. 39, 1500–1512. https://doi.org/10.1111/pce.12710.

Plascyk, J., Gabriel, F., 1975. The Fraunhofer Line Discriminator MKII – an airborne instrument for precise and standardized ecological luminescence measurement. IEEE Trans. Instrum. Meas. 24 (4), 306–313. https://doi.org/10.1109/TIM.1975.4314448.

Rascher, U., Agati, G., Alonso, L., Cecchi, G., Champagne, S., Colombo, R., Damm, A., Daumard, F., De Miguel, E., Fernandez, G., 2009. CEFLES2: the remote sensing component to quantify photosynthetic efficiency from the leaf to the region by measuring sun-induced fluorescence in the oxygen absorption bands. Biogeosciences 6, 1181–1198. https://doi.org/10.5194/bg-6-1181-2009.

Rascher, U., Alonso, L., Burkart, A., Cilia, C., Cogliati, S., Colombo, R., Damm, A., Drusch, M., Guanter, L., Hanus, J., Hyvarinen, T., Julitta, T., Jussila, J., Kataja, K., Kokkalis, P., Kraft, S., Kraska, T., Matveeva, M., Moreno, J., Muller, O., Panigada, C., Pikl, M., Pinto, F., Prey, L., Pude, R., Rossini, M., Schickling, A., Schurr, U., Schuttemeyer, D., Zemek, F., 2015. Sun-induced fluorescence - a new probe of photosynthesis: First maps from the imaging spectrometer HyPlant. Glob. Change Biol. 21, 4673–4684. https://doi.org/10.1111/gcb.13017 26146813.

Rossini, M., Burkart, A., Cogliati, S., Davies, N., Hom, M., Mac Arthur, A., Middleton, E., Rascher, U., 2016. Comparison of sun-induced chlorophyll fluorescence estimates obtained from four portable field spectroradiometers. Remote Sens. 8, 122. https://doi.org/10.3390/rs8020122.

Sabater, N., Vicent, J., Alonso, L., Verrelst, J., Middleton, E.M., Porcar-Castell, A., Moreno, J., 2018. Compensation of oxygen transmittance effects for proximal sensing retrieval of canopy–leaving sun–induced chlorophyll fluorescence. Remote Sens. 10, 1551. https://doi.org/10.3390/rs10101551.

Sager, J.C., McFarlane, J.C., 1997. Radiation. Plant growth chamber handbook. 1–29.

Smorenburg, K., Courrèges-Lacoste, G.B., Berger, M., Buschmann, C., Court, A., Del Bello, U., Langsdorf, G., Lichtenthaler, H.K., Sioris, C., Stoll, M.P., Visser, H., 2002. Remote sensing of solar induced fluorescence of vegetation. Int. Soc. Opt. Photonics 4542, 178–190. https://doi.org/10.1117/12.454193.

Tagliabue, G., Panigada, C., Dechant, B., Baret, F., Cogliati, S., Colombo, R., Migliavacca, M., Rademske, R., Schickling, A., Schüttemeyer, D., Verrelst, J., Rascher, U., Ryu, Y., Rossini, M., 2019. Exploring the spatial relationship between airborne-derived red and far-red sun-induced fluorescence and process-based GPP estimates in a forest ecosystem. Remote Sens. Environ. 231, 111272 https://doi.org/10.1016/j.rse.2019.111272.

van der Tol, C., Rossini, M., Cogliati, S., Verhoef, W., Colombo, R., Rascher, U., Mohammed, G., 2016. A model and measurement comparison of diurnal cycles of sun-induced chlorophyll fluorescence of crops. Remote Sens. Environ. 186, 663–677. https://doi.org/10.1016/j.rse.2016.09.021.

Westoby, M.J., Brasington, J., Glasser, N.F., Hambrey, M.J., Reynolds, J.M., 2012. 'Structure-from-Motion'photogrammetry: a low-cost, effective tool for geoscience applications. Geomorphology 179, 300–314. https://doi.org/10.1016/j.geomorph.2012.08.021.

Wyber, R., Malenovský, Z., Ashcroft, M.B., Osmond, B., Robinson, S.A., 2017. Do daily and seasonal trends in leaf solar induced fluorescence reflect changes in photosynthesis, growth or light exposure? Remote Sens. 9 (6), 604. https://doi.org/10.3390/rs9060604.

Xu, S., Liu, Z., Zhao, L., Zhao, H., Ren, S., 2018. Diurnal response of sun-induced fluorescence and PRI to water stress in maize using a near-surface remote sensing platform. Remote Sens. 10, 1510. https://doi.org/10.3390/rs10101510.

Yang, X., Shi, H., Stovall, A., Guan, K., Miao, G., Zhang, Y., Zhang, Y., Xiao, X., Ryu, Y., Lee, J.E., 2018. FluoSpec 2 – an automated field spectroscopy system to monitor canopy solar-induced fluorescence. Sensors 18, 2063. https://doi.org/10.3390/s18072063.

Zarco-Tejada, P.J., González-Dugo, M., Fereres, E., 2016. Seasonal stability of chlorophyll fluorescence quantified from airborne hyperspectral imagery as an indicator of net photosynthesis in the context of precision agriculture. Remote Sens. Environ. 179, 89–103. https://doi.org/10.1016/j.rse.2016.03.024.